Strain-induced ferroelectricity and spin-lattice coupling in SrMnO_{3} thin films

J. W. Guo, P. S. Wang, Y. Yuan, Q. He, J. L. Lu, T. Z. Chen, S. Z. Yang, Y. J. Wang, R. Erni, M. D. Rossell, V. Gopalan, H. J. Xiang, Y. Tokura, and P. Yu

Phys. Rev. B **97**, 235135 — Published 20 June 2018

DOI: 10.1103/PhysRevB.97.235135

Strain induced ferroelectricity and spin-lattice coupling in $SrMnO_3$ thin films

J. W. Guo[1*], P. S. Wang[2*], Y. Yuan[3*], Q. He[4#], J. L. Lu[2], T. Z. Chen[1], S. Z. Yang[1], Y. J. Wang[1], R. Erni[5], M. D. Rossell[5], V. Gopalan[3], H. J. Xiang[2,6#], Y. Tokura[7] and P. Yu[1,7,8#]

[1]State Key Laboratory of Low Dimensional Quantum Physics and Department of Physics, Tsinghua University, Beijing 100084, China

[2]Key Laboratory of Computational Physical Sciences (Ministry of Education), State Key Laboratory of Surface Physics, and Department of Physics, Fudan University, Shanghai 200433, China

[3]Department of Materials Science and Engineering and Materials Research Institute, Pennsylvania State University, University Park, Pennsylvania 16802, USA.

[4]Department of Physics, Durham University, Durham DH1 3LE, United Kingdom

[5]Electron Microscopy Center, Empa, Swiss Federal Laboratories for Materials Science and Technology, CH-8600 Dubendorf, Switzerland

[6]Collaborative Innovation Center of Advanced Microstructures, Nanjing 210093, P. R. China

[7]RIKEN Center for Emergent Matter Science (CEMS), Saitama, Japan

[8]Collaborative Innovation Center of Quantum Matter, Beijing 100084, China

***These authors contributed equally to this work.**

Correspondence to: qing.he@durham.ac.uk, hxiang@fudan.edu.cn and yupu@tsinghua.edu.cn

Designing novel multiferroic materials with simultaneous ferroelectric and magnetic orders has been one of the focal points over the last decade due to the promising applications and rich physics involved. In this study, using epitaxial strain (up to 3.8%) as a tuning knob, we successfully introduce novel multiferroicity with prominent high temperature ferroelectricity into the paraelectric $SrMnO_3$. More interestingly, the experimental temperature dependent ferroelectric and magnetic studies suggest that the emergent antiferromagnetic order below 100 K greatly enhances the ferroelectric polarization due to the spin-order induced ionic displacements. We envision that the strain mediated spin-phonon coupling can be utilized as a new pathway to discover novel functionalities in a wide range of antiferromagnetic insulators with delicate epitaxial manipulations.

Multiferroic materials with simultaneously ferroelectric and magnetic orders have attracted tremendous research interests because of their fundamental scientific importance as well as potential applications[1]-[5]. Accordingly, searching for novel multiferroic materials has been one of the central questions for related studies; among variable approaches (e.g. exploiting Bi 6s lone pairs[6], spin ordering[7], superlattice[8], octahedral rotation[9], etc.), strain engineering stands out as one of the most effective pathway[10]. Recent theoretical calculations have predicted that the external epitaxial strain can couple with the lowest frequency polar phonon and drive the antiferromagnetic-paraelectric $EuTiO_3$ into a ferromagnetic-ferroelectric multiferroic[11], which was later experimentally realized[12]. However, the low ferromagnetic transition temperature (~4 K) of $EuTiO_3$ due to its relatively low intrinsic Néel temperature limits its practical applications. Thus research focuses turn into materials with higher magnetic transition temperature, and it was theoretically proposed that epitaxial strain could stabilize the polar state in antiferromagnetic-paraelectric $SrMnO_3$ (SMO)[13] and other manganite systems[14],[15] and lead to superior multiferroicity with higher transition temperature. This prediction was soon confirmed in bulk SMO by partial substituting strontium with barium, which induced negative chemical pressure and led to a polar ferroelectric state[16]. Although rich phase diagram has been proposed recently for strained manganite sample from theoretical aspects[17][19], the experimental studies in SMO thin films and other related manganite system so far have been limited to small tensile strain cases (~1.6%)[20][25], and the study for larger tensile strain remains as a great challenge due to the difficulty to maintain the strain state of the film and obtain correct oxygen stoichiometry in synthesizing these samples[26][28].

In this work, high quality SMO thin films were successfully synthesized with tunable biaxial tensile strain (up to 3.8%) with selected substrates. With the highly strained sample, we observed the direct evidence of ferroelectricity with the ferroelectric transition temperature well above room temperature. The large remnant polarization (~55 $\mu C/cm^2$) observed strongly highlights the prominent ferroelectric performance as comparable to conventional ferroelectric materials. More interestingly, our studies reveal that in the highly strained samples, the emergence of the antiferromagnetic spin state (theoretically determined as C-type antiferromagnetic order) enhances the ferroelectric order as a consequence of the strong correlation between spin-lattice coupling and strain induced polar instability.

Results

Fabrication and characterization of highly strained $SrMnO_3$ thin films. Our experiments were performed on 10-nm-thick commensurate $(001)_{pc}$-oriented $SrMnO_3$ (SMO) films grown on $(001)_{pc}$ $(LaAlO_3)_{0.3}(Sr_2AlTaO_6)_{0.7}$ (LSAT), $(001)_{pc}$ $SrTiO_3$ (STO) and $(110)_o$ $DyScO_3$ (DSO) substrates with reflection high energy electron diffraction (RHEED) assisted pulsed laser deposition (PLD) method (**Supplementary Fig. 1**[29]). We note that the strained SMO thin film can very easily degrade in air by forming cracks in the film (as shown in **Supplementary Fig. 2**[29]), which will in turn relax the epitaxial strain and make it a big challenge to probe directly the intrinsic properties of this interesting material at a high strain state. To prevent the strained samples from degradation, we developed an 8-nm-thick $DyScO_3$ as a capping layer, which can make the films stable over a large scale of strain states. **Fig. 1a** shows typical X-ray diffraction (XRD) ***θ-2θ*** scans for SMO films grown on different substrates. The well-defined SMO diffraction peaks and clear Kiessig fringes indicate a high crystalline quality of the samples as well as their interfaces, which are also confirmed by the clear RHEED pattern and intensity oscillation during growth (**Supplementary Fig. 1**[29]**)**. Moreover, the cross-sectional scanning transmission electron microscopy (STEM) images (a typical image is shown in **Fig. 1b**) also reveal the film to be of highly commensurate and the interface is atomically abrupt. The sandwiched SMO layer was further investigated with rocking curve scans around the SMO (002) Bragg peak, and the full width at half maximum (~0.06°) is close to that of the substrates (~0.03°), implying a great crystallinity as well. To obtain the epitaxial relationship between SMO layers and substrates, reciprocal space mappings (**Fig. 1c** and **Supplementary Fig. 3**[29]**)** were performed. The close match of the in-plane lattice constants of the SMO layers to the corresponding substrates indicates the SMO samples being fully strained. With the knowledge on both in-plane and out-of-plane lattice constants, the tetragonality (c/a ratio) can then be obtained as shown in **Fig. 1d**, which is ~0.945 for the highly strained sample (SMO/DSO sample), providing a promising condition to introduce ferroelectricity.

Ferroelectricity in the highly strained samples. The optical second harmonic generation (SHG) measurements (see **Method** and **Supplementary Fig. 4**[29]) were carried out to detect the breaking of

inversion symmetry, which is a necessity to host ferroelectricity[30]. The fact that the STO substrate gives an enormous SHG background signal makes it impossible to study the SMO layer alone, thus only the results for SMO/DSO and SMO/LSAT samples are presented in **Fig. 2 (**as well as the following studies), from which well-defined SHG signals were obtained in the heterostructures, while both DSO and LSAT substrates give negligible contributions. The SHG polarimetry measurements of SMO/DSO were performed at both 4 K (**Fig. 2a** and **2b**) and room temperature (**Supplementary Fig. 5**[29]) by recording SHG signal while rotating the polarization of the fundamental beam. Theoretical modelling of the polarimetry results reveals a monoclinic symmetry of the system, suggesting that the electrical polarization not only has a large component along the pseudocubic <110> in-plane direction, but also a small [001] out-of-plane contribution.

We note that the breaking of inversion symmetry and arising of spontaneous polarization (P_1) can give SHG intensity in the form[31] of $I^{2\omega} \propto \chi_{ijkl}^2 P_1^2$, where χ_{ijkl} is susceptibility tensor allowed in the centrosymmetric parent phase. Thus, the temperature dependent polarization across the first-order transition can be written as, $P_l = P_0[\frac{1}{2} + \frac{1}{2}\sqrt{\frac{T_1 - T}{T_1 - T_c}}]$, where T_c is Curie temperature, T_1 is the upper bound of phase coexistence temperature. With these equations, temperature dependent SHG signal (**Fig. 2c**) can be further analyzed. Accordingly, SMO/LSAT exhibits a polar transition at T_c = 420 K with a fitting value of 433 K for T_1, which is very close to the ferroelectric transition obtained in the $Sr_{0.5}Ba_{0.5}MnO_3$ bulk [16] and SMO/LSAT thin film[24]. The nice agreement between experimental data and theory modelling suggests that the SHG signal from SMO/LSAT can be well explained by the emergence of spontaneous polarization below 420 K, while no other transition was observed. For the higher strained system, SMO/DSO, the SHG signal is clearly enhanced with the polar phase persists till 560 K, above which the film is irreversibly changed with the evidence shown in **Supplementary Fig. 7**[29]. Moreover, different from the case of the SMO/LSAT, the SHG signal of the SMO/DSO sample exhibits an interesting upturn around 120 K. Theoretical modelling by considering only one polar transition, P_1, with Curie temperature above 560 K, shows a clear disagreement below 120K. Interestingly, by introducing a second-order polar transition, P_2, at 120 K, the deviation between theory and experiment becomes smaller. However, according to DFT calculations presented later, the

magnitude of the second polarization (spin induced ferroelectric component) at 0 K is estimated to be $P_2 \approx 10\% P_1$. Thus, this large enhancement of SHG below 120 K cannot be explained only by the polar transitions. Since SMO is expected to establish antiferromagnetic ordering at low temperature, which is possible to dramatically enhance the SHG signal. By adopting the method in previous study[31], we consider the contribution of the antiferromagnetic order to the SHG as $I_{AFM}^{2\omega} \propto I_0^{2\omega}\left[1-\left(T/T_0\right)^{3/2}\right]^4$, where T_0 is the magnetic and polar orders coupling formation temperature. Taking this contribution into our model for SMO/DSO, we obtained a good agreement between theory and experiment with T_0 of 255 K. Note that although the magnetic ordering is likely to emerge simultaneous with P_2 at 120 K, this magnetic and polar coupling is proved to be able to persist into paramagnetic state, thus, well above magnetic transition temperature[31][32].

In order to further investigate the ferroelectricity of the strained SMO films, the ferroelectric hysteresis loops were measured by positive-up negative-down (PUND) method[33] with the interdigital electrode configuration as shown in the inset of **Fig. 2d**, from which only the remnant polarization is obtained. The measurement on SMO/DSO sample (**Fig. 2d**, in orange), reveals a well-defined hysteresis loop at 10 K with the remnant polarization (P_r) of ~55 μC/cm^2 along the in-plane direction. We note that this remnant polarization is comparable to conventional ferroelectric materials (e.g. $BaTiO_3$) suggesting the prominent ferroelectric nature of the highly strained sample. In contrast, the SMO/LSAT sample exhibits no loop behaviour with the electric field up to 30 kV/cm, above which the electric breakdown occurs with dramatically enhanced leakage current. To shed more light on the strain induced ferroelectric polarization, strain relaxed DSO/SMO/DSO sample (with the c/a ratio changed from 0.945 to 0.97) was also measured, in which however no remnant ferroelectric polarization was observed. This detailed comparison is consistent with the pervious LSDA+U result[13], which indicates that larger tensile strain (+3.6%) is desired to achieve the ferroelectricity in SMO.

Strain tuning of antiferromagnetic ordering and spin-lattice coupling in SMO films. The previous first-principle calculations[13] predicted that large tensile strain could drive the SMO film into a ferromagnetic state. However, macroscopic magnetic measurements on our present sample with strain up to 3.8 % (**Supplementary Fig. 8**[29]) shows no detectable remnant magnetization down to ~10 K,

indicating that the system remains its antiferromangetic state[34]. In order to investigate the magnetic nature of the highly strained SMO films, X-ray absorption spectroscopy (XAS) and X-ray linear dichroism (XLD) were employed to probe the antiferromagnetic state[35]. **Fig. 3a** (**Fig. 3b)** presents typical XAS of the Mn *L*-edges with the polarization (*E* field direction) of the incident light in close parallel (olive-green) and perpendicular (in orange) to the (001) direction of the crystal with the SMO/LSAT (SMO/DSO) films. The XLD spectra, as shown in **Fig. 3c** and **3d,** are then extracted from the difference between the XAS spectra taken with different polarizations. We note that the high-energy side of the Mn L_3 edge (between 643 eV and 648 eV) strongly overlaps with the Dy *M*-edges because of the second harmonic contamination of the beamline EPU; thus, only the spectra taken below 643 eV and over the L_2 edge were used for further analysis. For both SMO/LSAT and SMO/DSO samples, the turn-up of the Mn L_3 edge at the same energy position (~639 eV), and the almost identical characteristic energy for L_2 edge strongly suggest that the samples maintain good oxygen stoichiometry despite of the great different strain states.

We note that in some multiferroics, such as $BiFeO_3$, both antiferromagnetic and ferroelectric orders can contribute to the XLD signal[36]. Thus, temperature dependent XLD studies were employed here to separate their contributions. To avoid the second harmonic contamination of Dy from the capping layer, only the Mn L_2 edges were used for the studies, which show distinct XLD features at the characteristic energies of 651.4 eV and 652.7 eV (marked as A and B peaks in **Fig. 3c** and **3d**). The XLD amplitudes were then extracted using the asymmetry of the peak intensity between A and B peaks ($I_{XLD}=I_{A-B}/I_{A+B}$) and plotted in **Fig. 3e** as a function of temperature. The SMO/LSAT sample shows an obvious transition at ~160 K, while the SHG measurement reveals ferroelectric phase transition only at 420 K in this sample. Hence, in the current SMO system, the XLD signal is mainly attributed to the antiferromagnetic order, and the XLD transition temperature should be assigned as the antiferromagnetic Néel temperature (T_N=160 K), which shows excellent agreement to the previous experimental result[34]. In comparison, the XLD spectra on highly strained SMO/DSO sample show reversed features at the energies of 651.4 eV and 652.7 eV, pointing to a distinct antiferromagnetic easy axis from that of the SMO/LSAT. The corresponding temperature dependent result shows a transition at ~80 K, which can be attributed to the newly established antiferromagnetic transition according to the previous theoretical work[13] as well as

our theoretical analysis as discussed later. It is worth to note that the observed polar state well above 80 K by SHG doesn't contribute to significant XLD signal, which again suggests that the contribution of ferroelectric orders to the XLD is rather small. The coincidence of the transition temperature where the antiferromagnetic and enhanced ferroelectricity (**Fig. 2c**) emerge very likely indicates a strong coupling between the antiferromagnetic state and the great enhancement of the ferroelectric polarization at SMO/DSO sample.

First-principles density functional theory (DFT) calculations. In order to provide further theoretical insights into the magnetic and ferroelectric natures of the strained SMO films, first-principles DFT calculations (see **Method**) were carried out. Firstly, the distortions of the cubic perovskite parent phase (space group $Pm\bar{3}m$) of SMO were studied under various epitaxial strain states. For this purpose, global searches were performed for the lowest energy structures at each epitaxial strain based on the genetic algorithm (GA) specially designed to optimize structural distortions[37][38]. The calculated lattice constants and especially the strain dependent tetragonality show remarkable consistency with the experimental results (**Fig. 1d**). Then, the magnetic and ferroelectric ground states of the SMO films were further investigated at various strain states with the energy profile and ferroelectric polarization shown in **Fig. 4a** and **b**. The theoretical calculation predicts that SMO remains a G-type antiferromagnetic order for the small strain state, and then starts to favor C-type antiferromagnetic configuration at higher strains (**Fig.4a**). Moreover, the ferroelectric polarization is also predicted to be further enhanced with the larger strain state. For the bulk state, the SMO film is paraelectric because the lowest energy crystal structure has a C2/c non-polar symmetry; for the SMO films with tensile strain larger than 1% the lowest energy crystal structure turns into Ima2 for all magnetic states (**Fig. 4b**), which is consistent with the prediction by Lee and Rabe[13]. At the tensile strain of 3.8%, the calculated ferroelectric polarization is along the pseudo-cubic $[\bar{1}10]$ direction with the polarization magnitude of 47.11 $\mu C/cm^2$, in nice agreement with the experimental results. Because of the cubic symmetry of the bulk SMO and the biaxial tensile strain employed, there are four symmetrically equivalent <110> directions. Accordingly, the electric polarization could be along one of these four <110> axes, consistent with our SHG polarimetry. We note that SHG also suggests the existence of a small out-of-plane polarization along [001] direction, which is likely due to the presence of two inequivalent interfaces in the DSO capped heterostructure.

To shed a light on the magnetic nature of the highly strained sample, we constructed three-dimensional magnetic configurations by analysing the strain induced bond angle modulation as well as the consequent changes of nearest neighbour superexchange interactions and the next-nearest neighbour super-super-exchange interactions, as shown in **Supplementary Figs. 9**[29]. The results suggest that the magnetic ground state emerges into C-type antiferromagnetism, with the antiferromagnetic transition temperature T_N estimated by the mean field theory around 104 K for the SMO sample with 3.8% tensile strain (**Supplementary Notes 1** [29]and as shown in **Fig. 4c**), which is qualitatively consistent with the characteristic temperatures observed in SHG and XLD studies. The results can be explained in term of the Goodenough-Kanamori rule[39][40], where the antiferromagnetically coupled exchange interaction between d^3-d^3 ions is strongly suppressed and eventually changes into ferromagnetic interaction along the decreasing of the out-of-plane Mn-O-Mn bond angle with tensile strain (**Supplementary Figure 10**[29]). Note that we find that not only the Mn-O-Mn bond angle, but also the Mn-O bond length determines the nature of the Mn^{4+}-Mn^{4+} exchange coupling. To be more specific, a larger Mn-O bond length tends to favor a ferromagnetic Mn^{4+}-Mn^{4+} exchange coupling. This explains why the out-of-plane Mn-Mn exchange coupling becomes ferromagnetic when the Mn-O-Mn bond angle is still relative large (See **Supplementary Notes 2**[29] for details).

To understand the coupling between the antiferromagnetic state and ferroelectric polarization, we investigated the spin-order induced polarization. The ferroelectric polarization of the Ima2 SMO film at 3.8% strain with C-type antiferromagnetism is larger than that with G-type antiferromagnetism by ~4.69 $\mu C/cm^2$ (as shown in **Supplementary Fig. 11**[29]), and the enhanced polarization is along the same direction ($[\bar{1}10]$ direction) as the total polarization of the C-type and G-type antiferromagnetic phases (**Supplementary Fig. 12**[29]). We then carried out further analysis using the recently developed unified polarization model of spin-order induced polarization[41] to see which mechanism is mainly responsible for the enhancement of the electric polarization. Our DFT calculations reveal that the pure electronic, ion-displacement and lattice deformation contributions (i.e. P_e, P_{ion} and P_{def}) to the spin-order induced polarization enhancement can be estimated as 0.45 $\mu C/cm^2$, 4.30 $\mu C/cm^2$ and -0.06 $\mu C/cm^2$, respectively. Therefore, we can conclude that the ion-displacement contribution forms the dominated mechanism responsible for the spin-order induced polarization. We further investigated the underlying microscopic

mechanism by considering the spin-lattice energy, as discussed in detail in **Supplementary Note 3** and **Supplementary Figs. 13** and **14**[29]. We find the spin-order induced polarization by C-type antiferromagnetism is larger than that of G-type antiferromagnetism by 5.4 μC/cm^2, which is close to the direct DFT result (4.3 μC/cm^2). Our analysis demonstrates clearly that the oxygen ions move along the [1$\bar{1}$0] direction to minimize the ferromagnetic out-of-plane Mn-Mn exchange interaction energy in the C-type antiferromagnetic phase, which subsequently enhances the polarization along the [$\bar{1}$10] direction. Therefore, it can be concluded that the polarization enhancement below T_N is mainly due to the spin-order induced ions displacements (i.e., the exchange-striction mechanism[42][44]) in the C-type antiferromagnetic state with large tensile strain.

Summary

In summary, we have experimentally demonstrated the strain induced multiferroicity in SMO thin films showing simultaneous high temperature ferroelectricity and antiferromagnetism. The direct remnant ferroelectric hysteresis measurement reveals a polarization up to 55 μC/cm^2 at 10 K, on a par with the value of type-I multiferroic materials (e.g. $BiFeO_3$). Furthermore, the enhancement of ferroelectric polarization below the magnetic transition temperature for the highly strained samples suggests a spin-lattice coupling mechanism, in which the spin order leads to further ionic displacements and consequently enhancement of the ferroelectric polarization. Thus, the present study identifies strained SMO thin film as a novel high temperature multiferroic model system with intriguing magnetoelectric coupling. Finally, we expect that the strain mediated spin-phonon coupling can be well extended into a wide range of antiferromagnetic insulators with delicate epitaxial manipulation.

Methods

Thin film growth. High-quality epitaxial thin films were grown by the reflection high-energy electron diffraction (RHEED) assisted pulsed laser deposition (PLD) method. The SMO and DSO thin films were grown at 850 °C in a dynamic oxygen pressure of 0.15 mbar on various substrates enabling variable strain states. The laser energy (KrF, λ = 248 nm) was fixed at 1.4 J/cm^2 with repetition rate of 5 Hz. After the growth, the samples were cooled down to room temperature with 1 atm oxygen at cooling rate of 10 °C/min.

Structural characterization. The crystalline structure of thin films was analysed by the X-ray diffraction (XRD) and the reciprocal space mapping (RSM) measurements by four-circle X-ray diffractometer (Rigaku Smartlab). The sample for transmission electron microscopy measurements was prepared in cross-section by means of a FEI Helios Nanolab 450S focused ion beam (FIB) instrument. The high-resolution Z-contrast image was acquired in STEM mode with a HAADF detector using a double spherical aberration-corrected JEOL JEM-ARM200F microscope operated at 200 kV. The annular semi-detection range of the annular dark field detector was calibrated at 90-370 mrad.

Ferroelectric polarization measurements. Ferroelectric polarization hysteresis loops were measured using a Precision Multiferroic test system (Radiant Technologies). The in-plane ferroelectric polarization is probed through an interdigital electrode device geometry as shown in **Fig. 2d**. The length of interdigital electrodes is 575 μm, and the distance between the two electrodes is 5 μm, which is much larger than film thickness 10 nm. 50 nm Au with 10 nm Ti as buffer layer was employed as the electrode for the electric contact during the measurements. To avoid the possible leakage contribution, PUND method was employed to probe directly only the remnant polarization during the switching.

Second harmonic generation (SHG) measurements. The SHG response was measured with a far-field transmission geometry using an 800 nm fundamental laser beam generated by a Spectra-Physics SOLSTICE ACE Ti: Sapphire femtosecond laser system (<100 fs, 1 kHz). The experimental configuration is shown in **Supplementary Fig. 4**[29], where a linear polarized fundamental light is incident to the sample at a tilted angle of θ defined by the sample normal and optical axis. The second harmonic signal ($E_{2\omega}$) generated through the non-linear optical process within the sample is then

decomposed into *p*-polarized ($E_{2\omega//}$) and *s*-polarized ($E_{2\omega\perp}$) components by a polarizing beam-splitter. For each sample, SHG polar-plots were obtained by measuring the SHG response through rotating the incident polarization φ at fixed θ. Theoretical fitting of the SHG polarimetry data was performed by the method described in previous work[45], in which the nonlinear optical d_{ij} tensor for monoclinic symmetry was written as,

$$d_{ij}=\begin{pmatrix} 0 & 0 & 0 & 0 & d15 & d16 \\ d21 & d22 & d23 & d24 & 0 & 0 \\ d31 & d32 & d33 & d34 & 0 & 0 \end{pmatrix}.$$

Two sample orientations (O1 and O2) were employed during the measurements, which were defined as O1: {Z_1= [$\bar{1}$10], Z_2= [001], Z_3= [110]} and O2: {Z_1= [001], Z_2= [1$\bar{1}$0], Z_3= [110]} under DSO orthorhombic notation in our study. During simulations, we considered four possible domain configurations with mirror symmetry along one of the SMO pseudocubic (110), (1$\bar{1}$0), ($\bar{1}$10) or ($\bar{1}\bar{1}$0) planes. While for SMO/LSAT sample, two sample orientations were defined similarly as O1: {Z_1=[100], Z_2=[010], Z_3= [001]} and O2: {Z_1= [010], Z_2=[$\bar{1}$00], Z_3= [001]} under cubic notation of the LSAT substrate. Four possible domain configurations were then considered with mirror symmetry along LSAT cubic (110), ($\bar{1}$10), ($\bar{1}\bar{1}$0) and (1$\bar{1}$0) planes.

With these assignments, the SHG intensity can be described as:

$$\text{O1:}\begin{cases} I_{2\omega\|}^{\text{total}}=w_1 I_{2\omega\|}(\beta=45^\circ)+w_2 I_{2\omega\|}(\beta=135^\circ)+w_3 I_{2\omega\|}(\beta=225^\circ) \\ \quad +(1\text{-}w_1\text{-}w_2\text{-}w_3) I_{2\omega\|}(\beta=315^\circ) \\ I_{2\omega\perp}^{\text{total}}=w_1 I_{2\omega\perp}(\beta=45^\circ)+w_2 I_{2\omega\perp}(\beta=135^\circ)+w_3 I_{2\omega\perp}(\beta=225^\circ) \\ \quad +(1\text{-}w_1\text{-}w_2\text{-}w_3) I_{2\omega\perp}(\beta=315^\circ) \end{cases}$$

$$\text{O2:}\begin{cases} I_{2\omega\|}^{\text{total}}=w_1 I_{2\omega\|}(\beta=135^\circ)+w_2 I_{2\omega\|}(\beta=225^\circ)+w_3 I_{2\omega\|}(\beta=315^\circ) \\ \quad +(1\text{-}w_1\text{-}w_2\text{-}w_3) I_{2\omega\|}(\beta=405^\circ) \\ I_{2\omega\perp}^{\text{total}}=w_1 I_{2\omega\perp}(\beta=135^\circ)+w_2 I_{2\omega\perp}(\beta=225^\circ)+w_3 I_{2\omega\perp}(\beta=315^\circ) \\ \quad +(1\text{-}w_1\text{-}w_2\text{-}w_3) I_{2\omega\perp}(\beta=405^\circ) \end{cases}$$

where w_1,w_2,w_3,1-w_1-w_2-w_3 are volume fractions of the four possible domain configurations, $I_{2\omega\|}$ and $I_{2\omega\perp}$ are SHG intensities calculated from d_{ij} tensor after considering transmittance and reflectance, β is the sample rotation angle about its surface normal axis.

X-ray absorption and linear dichroism measurements. Soft X-ray absorption experiments were performed at Beamline I06 at the Diamond Light Source. The measurements were done with the incident angles of 30 degrees while tuning the polarizations of the linearly polarized light between horizontal and nearly vertical configurations. Due to existence of the DSO capping layer, bulk sensitive total fluorescence yield (TFY) mode was selected to probe the Mn *L* edges. The spectra normalization was done with the photon flux measured by the photocurrent of a clean gold mesh. The measurement temperature was set at the range from 3 K to 300 K.

First-principles calculations. The theoretical calculations were performed with the density functional theory (DFT) plus the on-site repulsion (U) method[46] within the generalized gradient approximation (GGA)[47] on the basis of the projector augmented wave (PAW) method[48][49] implemented in the Vienna ab initio simulation package (VASP)[50][51]. The PAW potentials explicitly include 10 valence electrons for Sr ($4s^2 4p^6 5s^2$), 13 for Mn ($3p^6 3d^5 4s^2$), and 6 for oxygen ($2s^2 2p^4$). The plane-wave cutoff energy was set to 500 eV. For the Brillouin zone sampling, a 4×4×3 k-point mesh was used for the 20-atom unit cell. Following previous DFT+U studies on $SrMnO_3$[13], the on-site repulsion (U) and exchange parameter (J) for Mn were chosen as 2.7eV and 1 eV, respectively. We adopted the original DFT+U formulation proposed by Liechtenstein *et al.*[46] to treat the 3d electron correlations in Mn. Note that Lee *et al.* adopted the simplified DFT+U formulation[52] proposed by Dudarev *et al.* To search for the lowest energy crystalline-structure, we adopted a global optimization method based on the genetic algorithm (GA) specially designed for finding the optimal structural distortion[37][38]. We note that our approach is different from the common GA algorithms in the following aspects: (1) To generate an initial structure of the first generation, we first randomly select a subgroup of the space group of the undistorted structure. By symmetrizing a structure with random distortions using the symmetry operation of the subgroup, an initial structure can be obtained with this selected subgroup symmetry. (2) For the mating operation, we propose another crossover operation besides the conventional cut-and-splice method. In our GA simulation, DFT was adopted to relax the structure and compute the total energy. In these DFT calculations, the G-type antiferromagnetic order was assumed. Our test calculations with the C-type antiferromagnetic order give to the same results. The number of atoms in the supercell was fixed to 20. The population size and number of generations were set to 24

and 15, respectively. After the GA global search, we then relaxed the obtained optimal structures with different magnetic order i.e. G-, A-, C-type antiferromagnetism, and ferromagnetism at each epitaxial strain state. The in-plane lattice constants were fixed while the out-plane lattice constant and the internal coordinates were fully optimized. For the calculation of ferroelectric polarization, the Berry phase method[53][54] was employed.

Acknowledgements

This work was financially supported by the National Basic Research Program of China (grant 2015CB921700) and National Natural Science Foundation of China (grant 11274194). Work at Durham was supported by the Engineering and Physical Sciences Research Council (grant EP/N016718/1). Work at Fudan was partially supported by Program for Professor of Special Appointment (Eastern Scholar), Qing Nian Ba Jian Program, and Fok Ying Tung Education Foundation. YY and VG were supported by the DOE DE-SC00012375 for his work on optical second harmonic generation.

References:

[1]. N. A. Spaldin & M. Fiebig, Science **309**, 391-392 (2005).
[2]. D. I. Khomskii, J. Mag. Mag. Mat. **306**, 1-8 (2006).
[3]. R. Ramesh and N. A. Spaldin, Nat. Mater. **6**, 21-29 (2007).
[4]. S. W. Cheong and M. Mostovoy, Nat. Mater. **6**, 13-20 (2007).
[5]. Y. Tokura, S. Seki and N. Nagaosa, Rep. Prog. Phys. **77**, 076501 (2014).
[6]. R. Seshadri and N. A. Hill, Chemistry of materials, **13**, 2892-2899 (2001).
[7]. T. Kimura, T. Goto, H. Shintani, K. Ishizaka, T. Arima and Y. Tokura, Nature **426**, 55-58 (2003).
[8]. J. A. Mundy, C. M. Brooks, M. E. Holtz, J.A. Moyer, H. Das, A. F. Rébola, J. T. Heron, J. D. Clarkson, S. M. Disseler, Z. Liu, A. Farhan, R. Held, R. Hovden, E. Padgett, Q.Mao, H. Paik, R. Misra, L. F. Kourkoutis, E. Arenholz, A. Scholl, J. A. Borchers, W. D. Ratcliff, R. Ramesh, C. J. Fennie, P. Schiffer, D. A. Muller and D. G. Schlom, Nature **537**, 523-527 (2016).
[9]. N. A. Benedek, A. T. Mulder and C. J. Fennie, J. Solid State Chem. **195**, 11-20 (2012).
[10].D. G. Schlom, L. Chen, C. J. Fennie , V. Gopalan, D.A. Muller , X. Pan , R. Ramesh and R. Uecker, MRS Bulletin, **39(02)**, 118-130 (2014).
[11].C. J. Fennie and K. M. Rabe, Phys. Rev. Lett. **97**, 267602 (2006).
[12].J. H. Lee, L.Fang, E. Vlahos, X. Ke, Y. W. Jung, L. F. Kourkoutis, J.W. Kim, P. J. Ryan, T. Heeg, M. Roeckerath, V. Goian, M. Bernhagen, R. Uecker, P. C. Hammel, K. M. Rabe, S. Kamba, J. Schubert, J. W. Freeland, D. A. Muller, C. J. Fennie, P. Schiffer, V. Gopalan, E. J. Halperin and D. G. Schlom, Nature **466**, 954-958 (2010).
[13].J. H. Lee and K. M. Rabe, Phys. Rev. Lett. **104**, 207204 (2010).
[14].S. Bhattacharjee, E. Bousquet and P. Ghosez, Phys. Rev. Lett. **102**, 117602 (2009).
[15].J. M. Rondinelli, A. S. Eidelson and N. A. Spaldin, Phys. Rev. B **79**, 205119 (2009).
[16]. H. Sakai, J. Fujioka, T. Fukuda, D. Okuyama, D. Hashizume, F. Kagawa, H. Nakao, Y. Murakami, T. Arima, A. Q. R. Baron, Y. Taguchi, and Y. Tokura, Phys. Rev. Lett. **107**, 137601 (2011).
[17].H. Chen and J. M. Andrew, Phys. Rev. B **94**(16) 165106 (2016).
[18].A. Marthinsen, C. Faber, U. Aschauer, N. A. Spaldin and S. M. Selbach, MRS Communications, **6**(3), 182-191 (2016).
[19].A. Marthinsen, S. M. Griffin, M. Moreau, T. Grande, T. Tybell, and S. M. Selbach, Phys. Rev. Materials **2**(1), 014404 (2018).
[20].C. Becher, L. Maurel, U. Aschauer, M. Lilienblum, C. Magén, D. Meier, E. Langenberg, M. Trassin, J. Blasco, I. P. Krug, P. A. Algarabel, N. A. Spaldin, J. A. Pardo and M Fiebig, Nat. Nanotechnology **10**, 661-665 (2015).
[21].R. Guzman, L. Maurel, E. Langenberg, A. R. Lupini, P. A. Algarabel, J. A. Pardo, and C. Magén, Nano Lett. **16**, 2221-2227 (2016).
[22].V. Goian, E. Langenberg, N. Marcano, V. Bovtun, L. Maurel, M. Kempa, T. Prokscha, J. Kroupa, P. A. Algarabel, J. A. Pardo, and S. Kamba, Phys. Rev. B **95**(7), 075126 (2017).
[23].E. Langenberg, L. Maurel, N. Marcano, R. Guzmán, P. Štrichovanec, T. Prokscha, C. Magén, P. A. Algarabel and J. A. Pardo, Adv. Mater. Interfaces, **4**(9), 1601040 (2017).
[24].S. Kamba, V. Goian, V. Skoromets, J. Hejtmánek, V. Bovtun, M. Kempa, F. Borodavka, P. Vaněk, A. A. Belik, J. H. Lee, O. Pacherová, and K. M. Rabe, Phy. Rev. B **89**(6), 064308 (2014).
[25].V. Goian, S. Kamba, F. Borodavka, D. Nuzhnyy, M. Savinov, and A. A. Belik, J. Appl. Phys. **117**(16), 164103 (2015).
[26].J. M. Rondinelli and N. A. Spaldin, S Adv. Mater **23**, 3363-3381 (2011).
[27].U. Aschauer, R. Pfenninger, S. M. Selbach, T. Grande, and N. A. Spaldin, Phys. Rev. B **88** 054111 (2013).
[28]. P. Agrawal, J. Guo, P. Yu, C. Hébert, D. Passerone, R. Erni, and M. D. Rossell, Phys. Rev. B **94**, 104101 (2016).
[29].See Supplementary Material at [URL will be inserted by publisher] for more details about structural characterization, measurements and calculation.
[30].R. C. Miller, Appl. Phys. Lett. **5**, 17-19 (1964).
[31].M. O. Ramirez, A. Kumar, S. A. Denev, N. J. Podraza, X. S. Xu, R. C. Rai, Y. H. Chu, J. Seidel, L. W. Martin, S.-Y. Yang, E. Saiz, J. F. Ihlefeld, S. Lee, J. Klug, S. W. Cheong, M. J. Bedzyk, O. Auciello, D. G. Schlom, R. Ramesh, J. Orenstein, J. L. Musfeldt, and V. Gopalan, Physical Review B **79**, 224106 (2009).
[32].P. A. Fleury, Physical Review, 180(2): 591(1969).
[33].J. F. Scott, C. A. Araujo, H. Brett Meadows, L. D. McMillan, and A. Shawabkeh, J. Appl. Phys. **66**, 1444 (1989).
[34]. L. Maurel, N. Marcano, T. Prokscha, E. Langenberg, J. Blasco, R. Guzmán, A. Suter, C. Magén, L. Morellón, M. R. Ibarra, J. A. Pardo, and P. A. Algarabel, Phys. Rev. B **92**, 024419 (2015).
[35].J. Stöhr and H. C. Siegmann, Springer, Berlin, Heidelberg, **5** (2006).

[36].M. B. Holcomb, L. W. Martin, A. Scholl, Q. He, P. Yu, C.-H. Yang, S. Y. Yang, P.-A. Glans, M. Valvidares, M. Huijben, J. B. Kortright, J. Guo, Y.-H. Chu, and R. Ramesh, Phys. Rev. B **81**, 134406 (2010).
[37].P. S. Wang, W. Ren, L. Bellaiche, and H. J. Xiang, Phys. Rev. Lett. **114**, 147204 (2015).
[38].X. Z. Lu, X. G. Gong and H. J. Xiang, Comput. Mater. Sci. **91**, 310 (2014).
[39].J. B. Goodenough, Phys. Rev. **100**, 564-573 (1995).
[40].J. Kanamori, J. Phys. Chem. Solids **10**, 87-98 (1959).
[41].H. J. Xiang, P. S. Wang, M.-H. Whangbo, and X. G. Gong, Phys. Rev. B 88, 054404 (2013).
[42].S. Picozzi, K. Yamauchi, B. Sanyal, I. A. Sergienko and E. Dagotto, Phys. Rev. Lett. **99**, 227201 (2007).
[43].X. Z. Lu, M. H. Whangbo, S. Dong, G. Gong and J. Xiang, Phys. Rev. Lett. **108**, 187204 (2012).
[44].G. Giovannetti, S. Kumar, C. Ortix, M. Capone and J. van den Brink, Phys. Rev. Lett. **109**, 107601 (2012).
[45].T. H. Kim, D. Puggioni, Y. Yuan, L. Xie, H. Zhou, N. Campbell, P. J. Ryan, Y. Choi, J.-W. Kim, J. R. Patzner, S. Ryu, J. P. Podkaminer, J. Irwin, Y. Ma, C. J. Fennie, M. S. Rzchowski, X. Q. Pan, V. Gopalan, J. M. Rondinelli and C. B. Eom, Nature **533**.7601 68-72(2016).
[46].A. I. Liechtenstein, V. I. Anisimov and J. Zaane, Phys. Rev. B **52**, R5467 (1995).
[47].J. P. Perdew, K. Burke and M. Ernzerhot, Phys. Rev. Lett. **77**, 3865-3868 (1996).
[48].P. E. Blöchl, Phys. Rev. B **50**, 17953–17979 (1994).
[49].G. Kresse and D. Joubert, Phys. Rev. B **59**, 1758–1775 (1999).
[50].G. Kresse and J. Furthmüller, Comput. Mater. Sci. **6**, 15–50 (1996).
[51].G. Kresse and J. Furthmüller, Phys. Rev. B **54**, 11169-11186 (1996).
[52].S. L. Dudarev, G. A. Botton, S. Y. Savrasov, C. J. Humphreys and A. P. Sutton, Phys. Rev. B **57**, 1505–1509 (1998).
[53].R. D. King-Smith and D. Vanderbilt, Phys. Rev. B **47**, 1651-1654 (1993).
[54].R. Resta, Rev. Mod. Phys. **66**, 899-915 (1994).

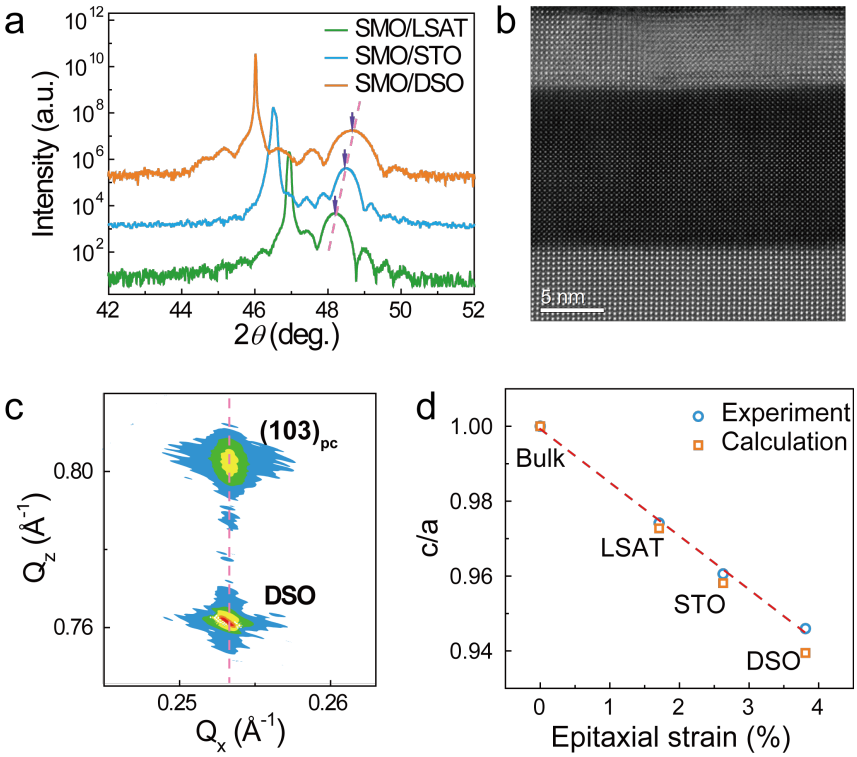

FIG. 1. Structural characterizations of high quality epitaxial thin films. (a) X-ray diffraction ***θ-2θ*** scans for SMO thin films grown on LSAT (green), STO (blue) and DSO (orange) substrates in the vicinity of out-of-plane $(002)_{pc}$ SMO reflection, where the subscript refers to the pseudocubic (pc) index. (b) Cross-sectional annular dark field image of the strained SMO thin film (dark region) grown on DSO substrate (bright regions). A thin DSO layer (top regions) was employed as capping layer. The image shows coherent growth between the SMO and DSO substrate with sharp interface and low density of defects within the film. (c) Reciprocal space mapping of the SMO film grown on the DSO substrate, demonstrating a coherent and epitaxial growth. (d) c/a ratio (tetragonality) of SMO films as a function of epitaxial strain. The orange square shows the DFT calculated results for comparison.

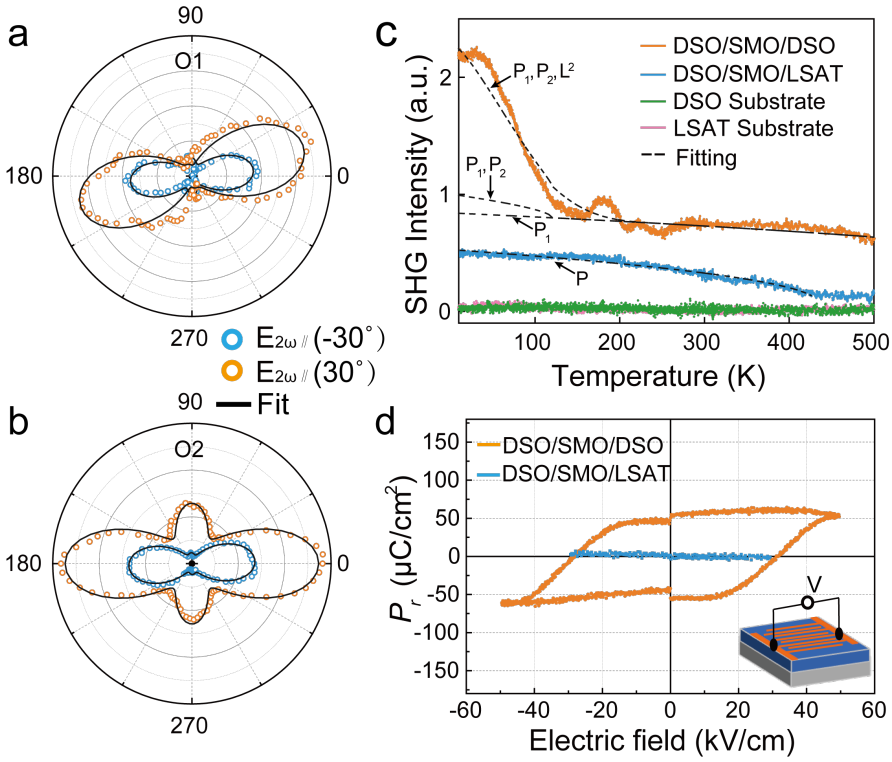

FIG. 2. Evidence of ferroelectricity in highly strained $SrMnO_3$ thin films. (a, b) Experimental SHG polar plots (at 4 K) of the highly strained SMO films grown on DSO substrates with sample orientations of O1 and O2, respectively. Domains with monoclinic symmetry were used in the fitting, which indicates the existence of both in-plane and out-of-plane polarization components. (c) Temperature dependent SHG response for SMO thin films grown on DSO (orange line) and LSAT (celeste line) substrates with reference data taken on bare DSO (green line) and LSAT (pink line) substrates. The dash lines show the fitting results using polar and magnetic model. (d) In-plane remnant ferroelectric hysteresis loops for SMO thin films grown on DSO (orange line) and LSAT (blue line) substrates measured at 10 K with the frequency of 1 kHz. The results were obtained with the PUND method, which probes directly the switchable and remnant ferroelectric polarization.

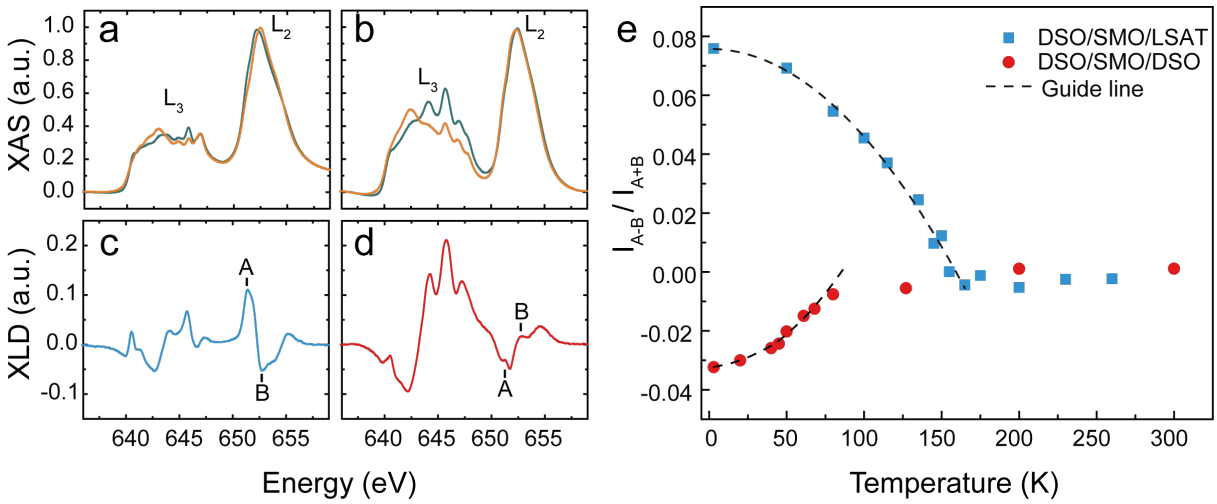

FIG. 3. The stain engineered magnetic orders in $SrMnO_3$ thin films. Representative Mn L-edge XAS results for SMO samples grown on (a) LSAT and (b) DSO substrates. The measurements were carried out at 3 K with the total fluorescence yield mode. Olive-green and orange lines represent the results with horizontal and vertical polarized X-ray, respectively. (c) and (d) represent the corresponding X-ray linear dichroism results. (e) Temperature evolution of the I_{XLD}, ratio of I_{A-B} to I_{A+B}. A and B represent the XLD intensities at 651.4 eV and 652.7 eV respectively.

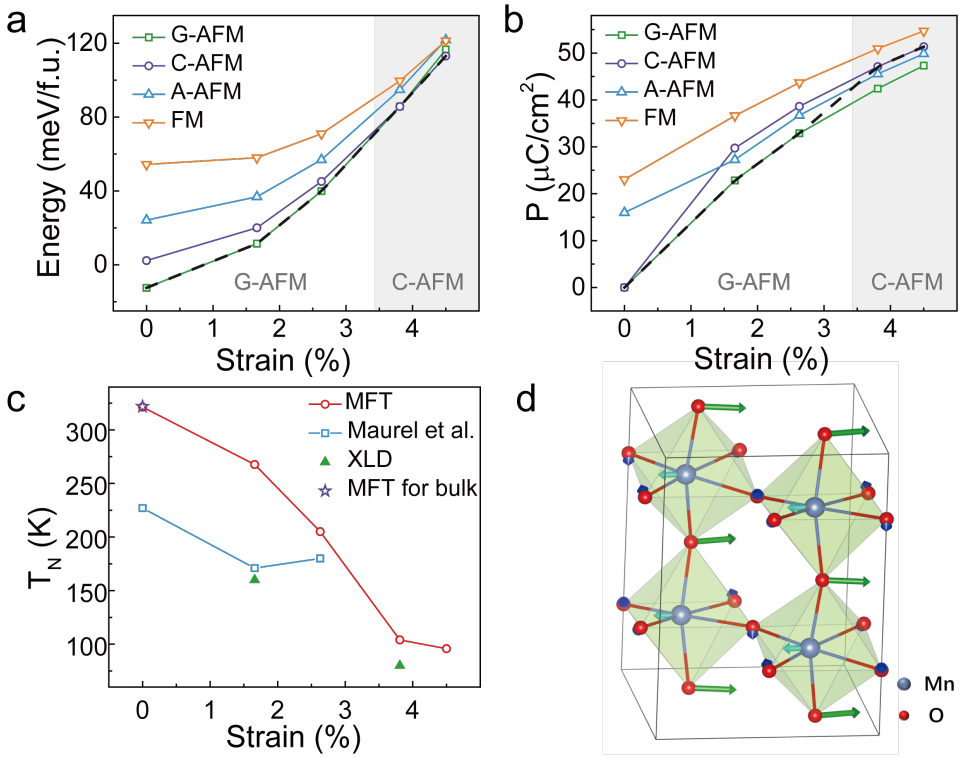

FIG. 4. First-principles calculations of ferroelectric and magnetic orderings in strained $SrMnO_3$ thin films. (a) Total energy of SMO as a function of epitaxial strain with different magnetic states. The cubic perovskite (i.e. space group $Pm\bar{3}m$) SMO with the G-type antiferromagnetic spin order is taken as the energy reference. Black dash line shows the magnetic ground states for different strains. (b) Ferroelectric polarizations of the lowest energy SMO structures with the G-type antiferromagnetic (green square), C-type antiferromagnetic (purple circle), A-type antiferromagnetic (blue triangle) and ferromagnetic (orange triangle) spin orders at different strain state. The polarization is along pseudo-cubic [$\bar{1}$10] direction. The black dash line shows the ferroelectric polarizations of the magnetic ground state. (c) Estimated magnetic transition temperatures (Néel temperature) of SMO at various strain states by the mean field theory. The blue square shows the previous experimental data[33] to compare with our mean field theory (MFT) results. The purple star shows Néel temperature of bulk unstrained SMO by the mean field theory. The green triangle represent the results from our XLD measurements. (d) Calculated crystalline structure of the 3.8% tensile strained SMO with Ima2 symmetry. The dark green vectors represent the ion displacements of the C-type antiferromagnetic state relative to that of the G-type antiferromagnetic state, which are along the pseudo-cubic [$\bar{1}$10] direction.